RSC Advances

PAPER

View Article Online
View Journal | View Issue

Cite this: *RSC Adv.*, 2026, **16**, 16442

Comprehensive study of the physical and optoelectronic properties of A_2AgIrF_6 (A = Cs, Rb, and K) double perovskites for energy harvesting applications: a DFT approach

M. A. Rayhan, *[abc] M. M. Hossain, [ab] M. M. Uddin[ab] and M. A. Ali *[ab]

In this study, we performed a comprehensive theoretical investigation of lead-free A_2AgIrF_6 (A = Cs, Rb, and K) double perovskites to examine their structural, electronic, optical, mechanical and thermodynamic properties using first-principles calculations. Known parameters, such as the Goldschmidt tolerance factor, octahedral factor and a novel tolerance factor (all indicating that these compounds are expected to form), were applied to validate the stability of the perovskite structure. Additional thermodynamic and dynamic stability checks, such as negative formation energies, positive phonon frequencies, and *ab initio* molecular dynamics (AIMD) simulations, strongly imply that these compounds can be synthesized experimentally. The band gaps derived from the Perdew–Burke–Ernzerhof Generalized Gradient Approximation (PBE-GGA) method for Cs_2AgIrF_6, Rb_2AgIrF_6, and K_2AgIrF_6 are 1.07 eV, 1.13 eV and 1.16 eV, respectively. We employed the Tran–Blaha modified Becke–Johnson (TB-mBJ) functional to adjust the band gaps. It yielded electronic band gaps of 1.65 eV, 1.76 eV and 1.83 eV for A_2AgIrF_6 (A = Cs, Rb, and K, respectively). The calculated band gaps are indirect and within the appropriate range for solar cell applications, as evidenced by density of states (DOS) studies. Optical property characterization showed that the solar cells based on all three perovskites could efficiently absorb visible light and achieve a peak absorption coefficient greater than 10^5 cm^{-1}, designating them as good absorbers. Mechanical behavior is determined through the analysis of elastic constants, and the compounds are found to be stable, ductile and anisotropic. In conclusion, A_2AgIrF_6 perovskites are highly promising, environmentally friendly candidates for use in optoelectronics and solar energy technologies. This theoretical research offers a crucial foundation for future experimental work and practical development.

Received 10th February 2026
Accepted 2nd March 2026

DOI: 10.1039/d6ra01202g

rsc.li/rsc-advances

1. Introduction

The world is using increasingly more energy, yet most of it comes from fossil fuels, which are running out and are harmful to the environment.[1,2] Solar energy and thermoelectric conversion are used to successfully harness sunlight and thermal energy, respectively, which are essential sources of power.[3] The selection of compounds plays a critical role in determining the performance of such photoelectric and thermal applications.[4]

Perovskite solar cells (PSCs) have been recently studied as a promising and low-cost next-generation solar cell technology, which can compete with or even replace silicon-based technologies.[5] PSCs were initially touted to have a moderate efficiency of up to 3.8% PCE, but research over the last decade has resulted in a record efficiency of 22.7%.[6,7] This development eclipses even the best-performing dye-sensitized solar cells (DSSCs), which took a little over 20 years to achieve an efficiency of 11.9%. The high performance of PSCs can be attributed to the unique features of the perovskite material, such as a superior charge carrier mobility, long diffusion length, tunable direct band gap, high absorption coefficient, low recombination rate and high molar extinction coefficient.[8] PSCs are third-generation solar cells that are cheap and efficient.[9–11] Furthermore, many studies have been dedicated to the photonic potential of the synthetic monolayer graphene, as other advanced technologies require its thermal stability.[12–14]

The chemical formula for perovskite materials is typically ABX_3, where A is a large cation, B is a smaller metal cation, and X represents an anion, typically a halogen or oxygen.[15] In perovskite structures, the A-site cation typically has a charge of +1, +2, or +3. The B-site cation usually has a charge of +2, +3, +4, or +5. The X-site anion generally carries a charge of −1 in

[a]*Department of Physics, Chittagong University of Engineering and Technology (CUET), Chattogram-4349, Bangladesh. E-mail: rayhan4302@gmail.com; ashrafphy31@cuet.ac.bd*

[b]*Advanced Computational Materials Research Laboratory (ACMRL), Department of Physics, Chittagong University of Engineering and Technology (CUET), Chattogram-4349, Bangladesh*

[c]*Department of Arts & Sciences, Bangladesh Army University of Science and Technology (BAUST), Saidpur Cantonment, Saidpur-5310, Nilphamari, Bangladesh*

halides and −2 in oxides. Lead-free double perovskites, on the other hand, have the structure $A_2B'B''X_6$, where A is a larger alkali metal cation (*e.g.*, Cs^+, Rb^+, and K^+), B′ is a monovalent cation such as Ag^+, B″ is a trivalent cation such as Ir^{3+}, and X is a halide ion. These halide-based double perovskites have the potential to serve as earth-abundant alternatives for conventional lead-containing perovskites in renewable optoelectronic and photovoltaic systems. In the context of photovoltaics, the stability and optoelectronic properties of this blend are considered attractive.[6] These materials have long carrier diffusion lengths, excellent thermal stability, and comparatively high absorption coefficients in the UV-vis range; in certain situations, the PCE can reach 25% or higher.[16,17] Lead-free double halide perovskites were identified as some more ecologically friendly options.

Double perovskites (DPs) are considered promising candidates for renewable energy because they hold the key to resolving challenges in global energy demand. Lead-free halide double perovskites have been proposed as promising and environmentally friendly alternatives to lead halide perovskites owing to the toxicity and structural instability of Pb. Pb-free halide double perovskites have recently attracted growing research interest for optoelectronic and photovoltaic applications because of their non-toxicity and improved stability.

Several experimental investigations have revealed the promising characteristics of halide double perovskites for PV applications. For instance, McClure *et al.*[18] prepared $Cs_2AgBiCl_6$ and $Cs_2AgBiBr_6$ materials through solid-state and solution methods and revealed that halide double perovskite semiconductors are environmentally friendly substitutes for lead halide perovskites. Similarly, Wei *et al.*[19] manifested the lead-free double perovskite $Cs_2AgSbBr_6$ as a potential photovoltaic absorber, with an indirect optical band gap of 1.64 eV (bulk crystals) and 1.89 eV (thin films), relevant for solar energy conversion. Zhang *et al.*[20] synthesized a new cost-effective double perovskite Cs_2NaBiI_6 using a facile hydrothermal process and found it to exhibit good stability and repeatability for fabricating devices, which satisfies the demands of photovoltaic applications. Mustafa *et al.*[21] synthesized Cs_2AgAsX_6 materials with band gaps varying from 1.0 to 1.9 eV, indicating good visible light absorption and possible sunlight conversion.

Theoretical studies have further demonstrated that halide double perovskites are promising materials for photovoltaic and optoelectronic applications. Alotaibi *et al.*[22] reported the mechanical, optical, thermoelectric and thermodynamic properties of Cs_2AgBiX_6 (X = Cl and Br), indicating its feasibility for renewable energy applications. Saeed *et al.*[23] studied the first-principles calculations of Cs_2AgCrX_6 (with X = Cl, Br, and I) for possible optoelectronic applications. Maryam *et al.*[24] calculated the band structures of Cs_2AgSbX_6 (X = Cl, Br, and I) using density functional theory (DFT) and concluded that it was a promising Pb-free semiconductor for solar cells. Anbarasan *et al.*[25] studied Cs_2AgInX_6 (X = Cl, Br, and I) and identified its applicability as a single-junction solar cell from its corresponding physical and photovoltaic attributes. Nazir *et al.*[26] further investigated the optical, electronic and thermoelectric profiles of Rb_2AgAsX_6 (X = Cl, Br, and I), affirming its use for optoelectronic purposes. Ali *et al.*[27] suggested that new double perovskites K_2AgAsX_6 (X = Cl and Br) can be considered for different energy-related technologies. Similarly, Zanib *et al.*[28] proposed K_2AgAsX_6 (X = Cl and Br) with strong visible light absorption properties as possible solar cell and thermoelectric materials. The structural and optoelectronic properties, and the band gap of Rb_2AgBiI_6 in the visible region of the electromagnetic spectrum, were later established by Bhorde *et al.*[29] In addition, several first-principles studies on lead-free sodium-based double perovskites have demonstrated their structural, optoelectronic, and thermoelectric potential for eco-friendly solar and thermoelectric applications.[30–35]

Motivated by the above findings, we employed density functional theory (DFT) to investigate a new series of double perovskites with the general formula A_2AgIrF_6 (A = Cs, Rb, and K). Previous studies have underscored the potential of halide double perovskites in environmentally friendly energy technologies. In this work, we explore the structural, electronic, optical, mechanical, and thermodynamic properties of A_2AgIrF_6 (A = Cs, Rb, and K) compounds using the WIEN2k computational package. As far as we know, no experimental/theoretical work has been reported for these compounds. The calculation results show that A_2AgIrF_6 (A = Cs, Rb, and K) double perovskites are promising candidates for photovoltaic and energy conversion devices owing to their tunable band gap. The results of this work are anticipated to be helpful in the continuous improvement of lead-free double perovskites and for future experimental/theoretical research of these materials in terms of energy applications.

2. Computational methods

Using DFT-based simulations with the Wien2k code, the structural, electronic, thermal, optical, and mechanical properties of the A_2AgIrF_6 DHP compound are analyzed. To solve the Kohn–Sham (KS) equations, the Full-Potential Linearized Augmented Plane Wave (FP-LAPW) method, along with local orbitals, is employed.[36] The structural properties are determined using the GGA-PBE exchange-correlation potential.[37] Since GGA-PBE underestimates the band gap, the TB-mBJ potential[38] is applied after GGA-PBE to correct this discrepancy.[39] For the wave functions inside muffin-tin spheres, the basis set comprises spherical harmonics of up to the angular momentum $l_{max} = 10$. In the interstitial region, a plane-wave basis set is used, with a cut-off value of $R_{MT}k_{max} = 7$. For Brillouin zone integration for polygons and naked PES, the Monkhorst–Pack k-mesh[40] consisting of 1000-k points is employed for the calculation of electronic and optical properties. In this work, the stabilization criterion of the energy up to 10^{-4} Ry and the charge up to 0.001e is used. During mechanical property calibration, we calculate the elastic constants. The Wien2k code utilizes two packages to analyze mechanical and optical properties: elastic and optic. These analyses provide insights into the mechanical stability and optical traits of DHP based on the electronic structure of the DHP compound, thereby comprehensively establishing its characteristics.

3. Results and discussion

3.1. Structural parameters and stability

The double halide perovskite (DHP) materials, which are of the form A_2AgIrF_6 (A = Cs, Rb, and K), adopt a face-centered cubic structure with space group $Fm\bar{3}m$ (no. 225).[41] It contains [AgF_6] and [IrF_6] octahedra where the A-site cations (Cs, Rb, and K) reside in their interstices to hold the crystal lattice as a whole, as shown in Fig. 1. Specifically, the A-site cations occupy the 8c Wyckoff position (0.25, 0.25, 0.25), Ag is located at the 4a position (0.5, 0.5, 0.5), Ir is at the 4b position (0, 0, 0), and F is at the 24e position (0.25, 0, 0). Geometry optimization was carried out to evaluate the stability and structural properties of the materials. The lattice constants (a_0), bulk moduli (B_0), and total energies (E_{tot}) of each compound are tabulated in Table 1. The results show a continuous decrease in the lattice constant with increasing A-site cation from Cs to K, in good agreement with the well-established ionic-radii sequence (Cs > Rb > K). Importantly, the existing literature does not contain experimental evidence that directly shows the novelty of these findings.

The thermodynamic stability of A_2AgIrF_6 was confirmed by determining the formation energy (E_f) and binding energy (E_b) using the following equations:[42]

$$E_f = \frac{E_{A_2AgIrF_6} - n_A \times E_A - n_{Ag} \times E_{Ag} - n_{Ir} \times E_{Ir} - n_F \times E_F}{40} \quad (1)$$

and

$$E_b = \frac{E_{A_2AgIrF_6} - n_A \times \mu_A - n_{Ag} \times \mu_{Ag} - n_{Ir} \times \mu_{Ir} - n_F \times \mu_F}{40}, \quad (2)$$

where $E_{A_2AgIrF_6}$ represents the overall energy of the compound in the final state and E_A, E_{Ag}, E_{Ir}, and E_F are energies of the respective atoms. The negative energies of E_f and E_b calculated in this work (as presented in Table 1) can further attest to the thermodynamic stability of these compounds, which indicates their potential for synthesis.

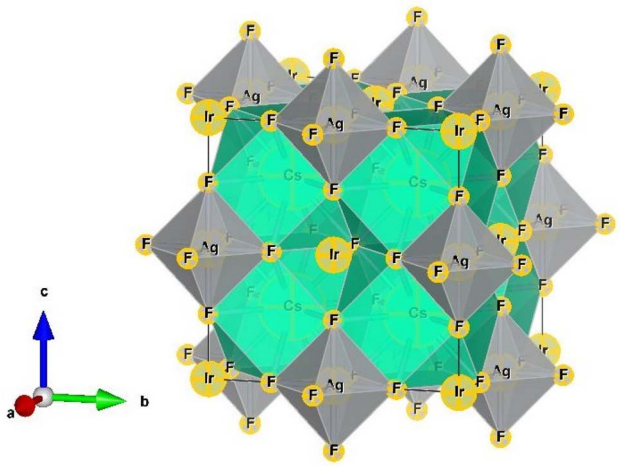

Fig. 1 Unit cell of Cs_2AgIrF_6.

Table 1 Lattice constant a_0 (Å), bulk modulus B_0 (GPa), pressure derivative B_0', total energy E_{tot} (Ry), formation energy E_f (eV per atom) and binding energy E_b (eV per atom) for double perovskite (DP) A_2AgIrF_6 (A = Cs, Rb, and K)

DP	a_0 (Å)	B_0 (GPa)	B_0'	E_{tot} (Ry)	E_f (eV per atom)	E_b (eV per atom)
Cs_2AgIrF_6	8.88	68.87	5.32	−78711.02	−3.77	−5.33
Rb_2AgIrF_6	8.75	72.80	4.44	−59475.81	−3.73	−5.33
K_2AgIrF_6	8.68	72.22	5.48	−49958.38	−3.69	−5.33

Crystallographic stability was further validated by calculating the octahedral factor (u), Goldschmidt tolerance factor (t), and the new tolerance factor (τ) using the following equations:[43–45]

$$t = \frac{(R_A + R_F)}{\sqrt{2}(R_B + R_F)}, \quad (3)$$

$$u = \frac{R_B}{R_F} \quad (4)$$

and

$$\tau = \frac{R_F}{R_B} - n_A\left(n_A - \frac{R_A/R_B}{\ln(R_A/R_B)}\right), \quad (5)$$

where R_A, R_B, and R_F are the symbols for the ionic radii of ions A, B, and F, respectively. All the parameters listed in Table 2 have been evaluated and found to lie within the stability range,[46] which corroborates the crystallographic stability of the compounds.

A set of structural calculations for A_2AgIrF_6 was performed with varying unit cell volume and cubic symmetry to evaluate the stability and structural performance. To characterize the pressure–volume correlation, Birch–Murnaghan equation of state was applied to describe the pressure-volume-total energy relationship. The resulting volume optimization curves illustrated in Fig. 2 indicate the total energy relative to volume. The equilibrium volume and ground state energy of each compound corresponds to the bottom of those curves. The findings, as anticipated, indicate a relationship between the ionic radius of the A-site cation and the equilibrium volume, with a larger volume observed for Cs_2AgIrF_6 and a comparatively smaller volume for K_2AgIrF_6. This work highlights the prospect of the discussed computational method and provides a strong basis for further examinations of the structural and stability properties of such systems.

3.2. Phonon stability

Structural stability evaluation is essential for predicting the viability of new compounds. Thus, we systematically studied the vibrational properties of the A_2AgIrF_6 compounds. The phonon dispersion curves (PDC) and PDOS of A_2AgIrF_6 (A = Cs, Rb, and K) were calculated using the finite displacement method (FDM)[47] with the CASTEP package.[48] Structural relaxation was performed over a 2 × 2 × 2 supercell, with an atomic

Table 2 Calculated parameters including Shannon's ionic radii (r), Goldschmidt tolerance factor (t), octahedral factor (u), and new tolerance factor (τ) for the A_2AgIrF_6 (A = Cs, Rb, and K) compounds

DP	Ionic radius of cations (Å)		Ionic radius of anion (Å)	Tolerance factor (t)	Octahedral factor (u)	New tolerance factor (τ)
	r_A	$(r_{Ag} + r_{Ir})/2$	r_F			
Cs_2AgIrF_6	1.88	0.92	1.33	1.01	0.69	3.32
Rb_2AgIrF_6	1.72	0.92	1.33	0.96	0.69	3.47
K_2AgIrF_6	1.64	0.92	1.33	0.93	0.69	3.52

displacement of 0.01 Å. The PDCs and PDOS are displayed in Fig. 3, obtained at high-symmetry point (W–L–Γ–X–W–K) parameters, and exhibited no negative phonon frequencies, indicating that all the compounds are stable under natural conditions. Since the unit cell of these compounds contains 40 atoms, the vibrational spectrum includes 120 branches. Three of these are acoustic modes, which describe the collective movements of the crystal lattice, and the remaining 117 are higher-energy optical modes. The data in Fig. 3 do not exhibit such soft modes, supporting the fact that A_2AgIrF_6 structures are dynamically stable and can be synthesized. Phonon DOS analysis provides the vibrational contributions of each atom. Cs_2AgIrF_6 and Rb_2AgIrF_6 show PDC curves in the 0–16 THz range, while K_2AgIrF_6 reaches up to 18 THz. Low-frequency modes are mainly contributed by the A-site cations (Cs, Rb, and K), and atoms with high frequency are dominated by Ir and F atoms.

In addition to vibrational stability, thermal stability is important. The thermal stability was verified from the *ab initio* molecular dynamics (AIMD) simulations carried out in an NVT ensemble at room temperature (300 K). Fig. 4 shows the evolution of the total energy over time for the three compounds under investigation. In the case of Cs_2AgIrF_6, the plot is shown in Fig. 4(a), and the energy is going down, ranging from −177.63 eV to −174.99 eV for all systems. The average energy (−176.54 eV) and percentage error from the highest to lowest (0.29% and 0.41%) show the strong thermal stability of the compound. The energy response of Rb_2AgIrF_6 is shown in

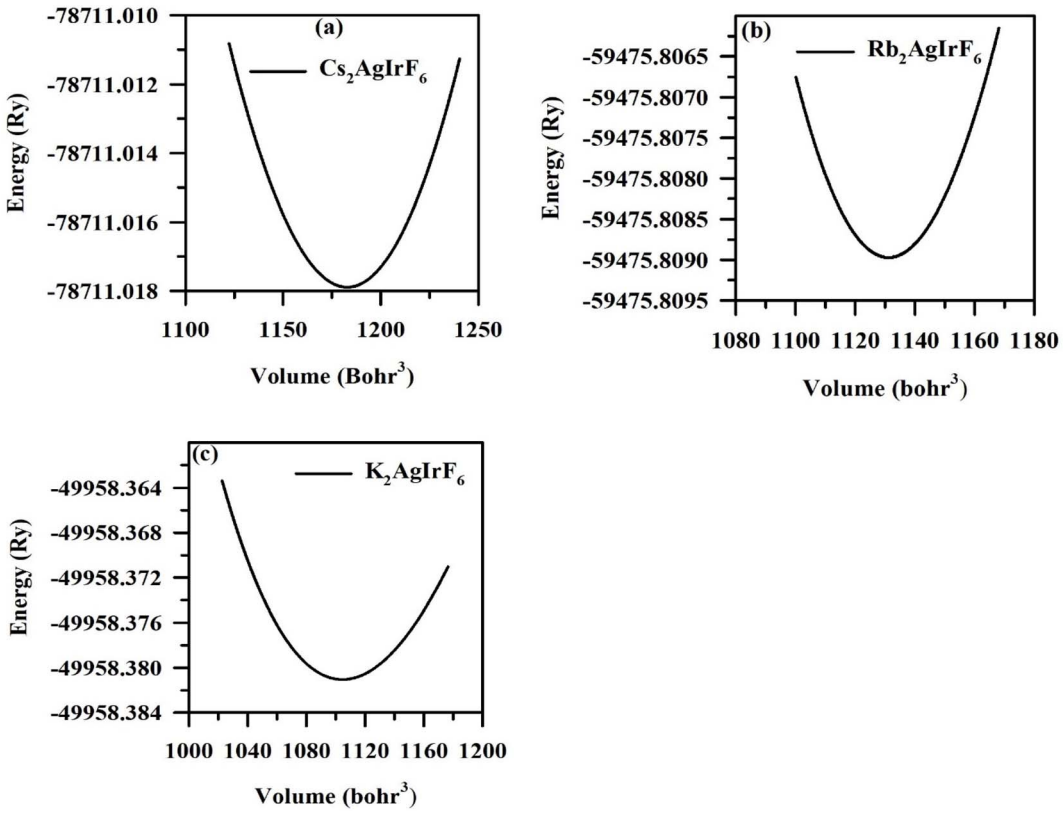

Fig. 2 Total energy *vs.* volume curves for the (a) Cs_2AgIrF_6, (b) Rb_2AgIrF_6, and (c) K_2AgIrF_6 compounds fitted using the third-order Birch–Murnaghan equation of state.

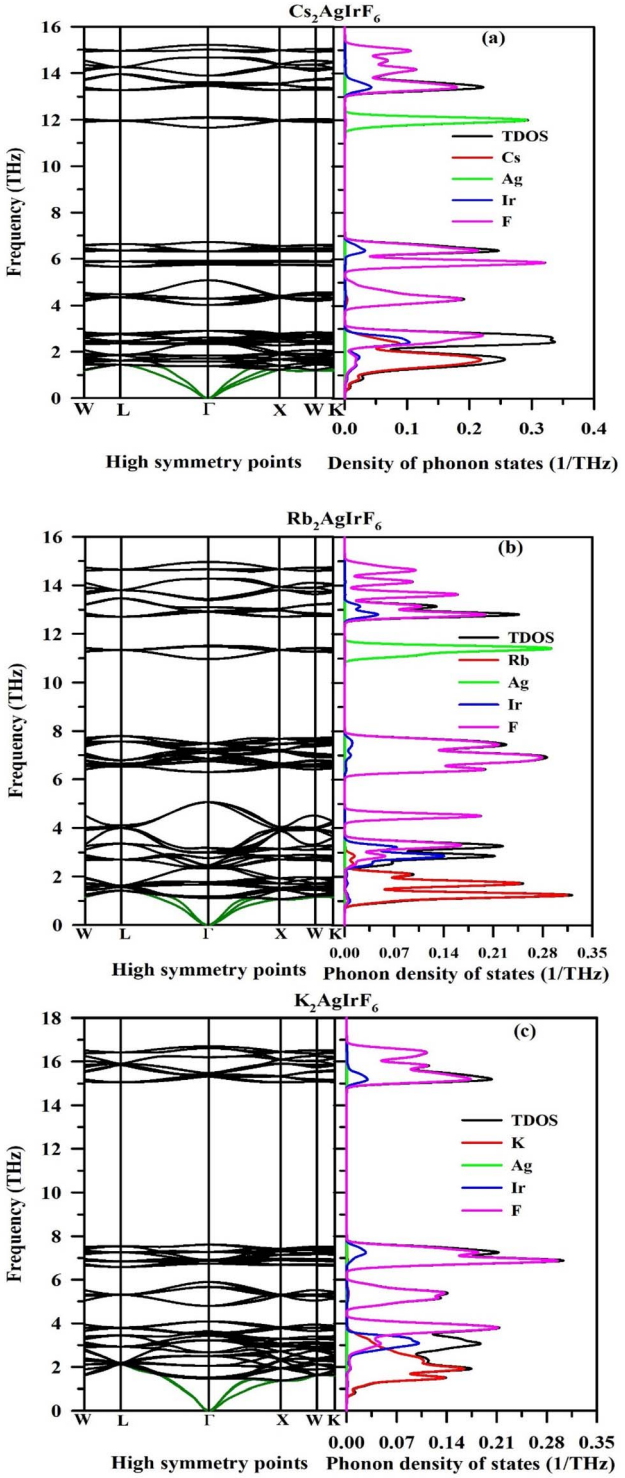

Fig. 3 PDCs with phonon DOS of the (a) Cs_2AgIrF_6, (b) Rb_2AgIrF_6, and (c) K_2AgIrF_6 compounds.

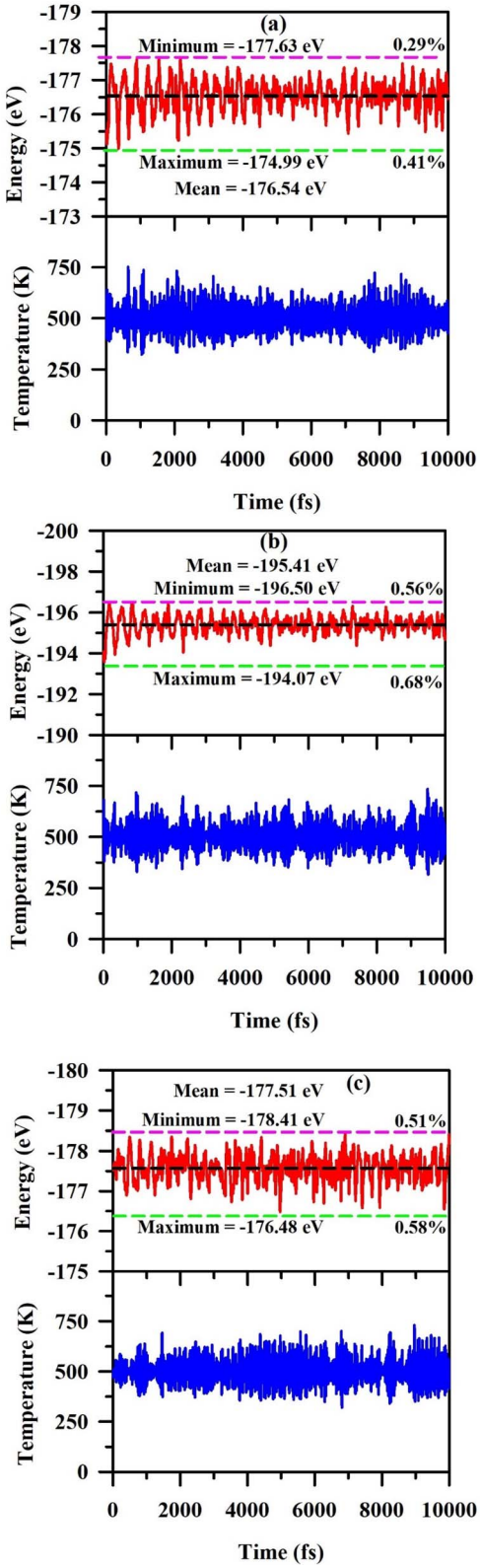

Fig. 4 Variation in the energy profiles and temperature as a function of the time step (fs) for the (a) Cs_2AgIrF_6, (b) Rb_2AgIrF_6, and (c) K_2AgIrF_6 compounds.

Fig. 4(b), with changes in a narrow range between −196.50 and −194.07 eV, with an average of −195.41 eV. The offsets from the mean yield 0.56% (between the minimum and mean) and 0.68% (between the maximum and mean). These minor changes point to the stability features of the compound

regarding its thermal properties. Fig. 4(c) shows that the energy of the third compound K_2AgIrF_6 lies between −178.41 eV and −176.48 eV, averaging at −177.51 eV. The differences from the minima and the maxima to the mean are 0.51% and 0.58%, respectively. The smooth and steady trend observed in this energy profile is a sign of strong dynamic stability. This stability is further supported by enhanced phonon scattering, which helps protect the structure from failing.

3.3. Electronic properties

DFT calculations are effective for studying the electronic properties of materials, including band structure, mobility, and density of states. The arrangement of the electronic distribution across an energy level in a material, represented in the band structure, helps in defining the nature of a material as either a conductor, insulator, or semiconductor.[49] Simplified energy dispersion and density of states are very useful in electronic and optoelectronic applications. One of these parameters is the band gap, which shows the range of energies within the solid and provides details on the electrical characteristics of the material. The band profile is shown in Fig. 5.

The left panel of Fig. 5 illustrates the band structure calculated using the GGA-PBE method, while the right panel displays the band structure calculated with the TB-mBJ method. The Fermi level is set to 0 eV to facilitate the comparison of the bandgaps for both models. The calculated band gap values for Cs_2AgIrF_6, Rb_2AgIrF_6, and K_2AgIrF_6 are 1.07 (1.65) eV, 1.13 (1.76) eV, and 1.16 (1.83) eV, respectively, as obtained using the GGA-PBE (TB-mBJ) functional and summarized in Table 3. The gradual increase in the band gap from Cs_2AgIrF_6 to Rb_2AgIrF_6 and K_2AgIrF_6 is attributed to the decreasing ionic radius of the A-site cation, which induces lattice contraction and greater distortion of the AgF_6 and IrF_6 octahedra. Such structural modifications weaken the orbital hybridization among the Ag-4d, Ir-5d, and F-2p states, thereby reducing band dispersion and widening the band gap. Hence, replacing Cs with smaller Rb and K ions enhances octahedral distortion and leads to a systematic increase in the electronic band gap.

The figures show that the TB-mBJ method outperforms the GGA-PBE by correcting its errors of underestimating band gaps. Band structure calculations were performed along the Brillouin zone path at the high-symmetry points that included *W* (0.50, 0.25, 0.75), *L* (0.5, 0.5, 0.5), *Γ* (0, 0, 0), *X* (0.5, 0, 0), *W* (0.50, 0.25, 0.75), and *K* (0.375, 0.375, 0.75). Both profiles portray a parabolic nature at the conduction band minimum and valence band maximum.

Fig. 5 reveals that the conduction band minimum (CBM) and valence band maximum (VBM) occupy distinct symmetry points, confirming the indirect bandgap nature of all double perovskites (DPs). According to the Shockley–Queisser (S–Q) model, semiconductor materials require an optimal bandgap of ~1.4 eV to achieve maximum theoretical efficiency in single-junction photovoltaic cells under standard solar illumination.[52] In addition, the band gap of perovskite within the range of 0.8–2.2 eV makes the perovskite suitable for the photosensitive electrochemical (PEC) process.[53] The band gap values

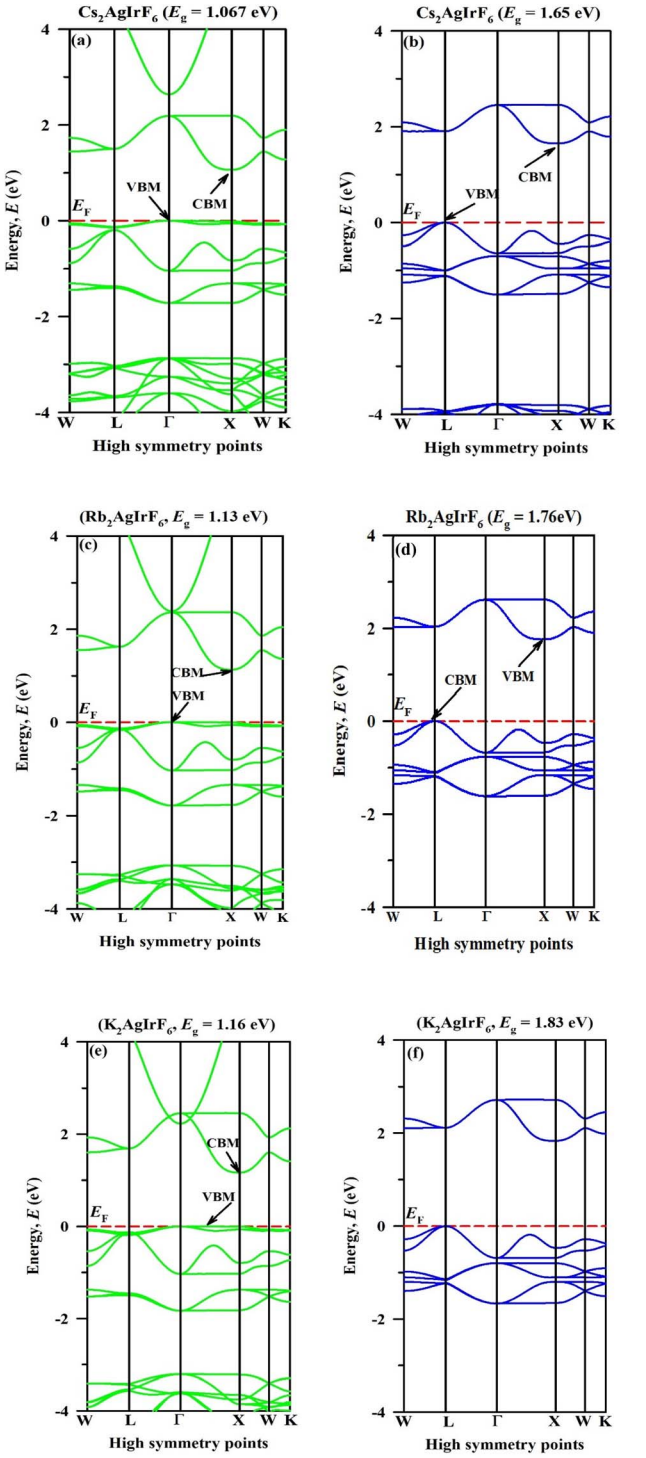

Fig. 5 Band structure of the (a) Cs_2AgIrF_6 (GGA PBE), (b) Cs_2AgIrF_6 (TB-mBJ), (c) Rb_2AgIrF_6 (GGA PBE), (d) Rb_2AgIrF_6 (TB-mBJ), (e) K_2AgIrF_6 (GGA PBE), and (f) K_2AgIrF_6 (TB-mBJ) compounds.

calculated for Cs_2AgIrF_6, Rb_2AgIrF_6, and K_2AgIrF_6 are also within the ideal range of SQ values, and from the aspect of photosensitivity, they can be named as a highly photosensitive material for higher optoelectronics applications.

Table 3 Computed energy band gaps, band gap types, and electron/hole effective mass values for the A_2AgIrF_6 (A = Cs, Rb, and K) DHP compounds

Compounds	Band gap (eV)	Functional	Type	Effective mass of electron, m_e^*	Effective mass of hole, m_h^*	Reference
Cs_2AgIrF_6	1.07	GGA PBE	Indirect	0.46 m_e	3.64 m_e	This work
	1.65	TB-mBJ	Indirect	0.29 m_e	0.99 m_e	
Rb_2AgIrF_6	1.13	GGA PBE	Indirect	0.47 m_e	4.98 m_e	This work
	1.76	TB-mBJ	Indirect	0.28 m_e	0.94 m_e	
K_2AgIrF_6	1.16	GGA PBE	Indirect	0.38 m_e	6.20 m_e	This work
	1.83	TB-mBJ	Indirect	0.27 m_e	0.84 m_e	
Cs_2AuAsF_6	0.518	GGA-PBE	Indirect	—	—	50
	1.144	TB-mBJ	Indirect	0.16 m_e	0.48 m_e	
Cs_2AuSbF_6	0.777	GGA-PBE	Indirect	—	—	50
	1.746	TB-mBJ	Indirect	0.25 m_e	0.72 m_e	
$Cs_2NaIrCl_6$	0.92	GGA-PBE	Direct	0.21 m_e	1.33 m_e	51
	1.93	TB-mBJ	Direct	0.30 m_e	1.69 m_e	
$Rb_2NaIrCl_6$	0.97	GGA-PBE	Direct	0.20 m_e	1.10 m_e	51
	2.02	TB-mBJ	Direct	0.29 m_e	1.41 m_e	

m_e = mass of electron.

The effective mass of charge carriers is the effective mass of electrons or holes in materials like double perovskite halides. It elucidates the behavior of charge carriers and how they respond to stimuli, including electric fields. In DHPs, the effective mass depends on the curvature of the band structure of a material and the composition of the frame of the perovskite based on halides and other elements.

For the compounds, A_2AgIrF_6 (A = Cs, Rb, and K), the effective masses of holes and electrons were evaluated at high-symmetry points corresponding to the CBM and VBM. The effective mass m^* was determined using the following expression:[54]

$$m^* = \frac{\hbar^2}{\left(d^2\varepsilon(k)/dk^2\right)}, \quad (6)$$

where m^* refers to the effective mass of the charge carrier and $\hbar$ is less known as the reduced Planck constant. In contrast, $\varepsilon(k)$ and $d^2\varepsilon(k)/dk^2$ refer to the energy eigenvalue and the second derivative of $\varepsilon(k)$ concerning wave vector k, respectively.

In the case of m^*, this equation suggests that the value is directly proportional to the dispersion curve of the electronic band. The calculated effective mass values are provided in Table 3, which are several orders of magnitude lower than those considered for other DHPs.[55,56] These carriers have a lower effective mass, increasing the carrier mobility essential for charge transport. In addition, the carrier mobility is a function of the ratio of hole mass to electron mass (m_h^*/m_e^*). However, the increase in the effective mass decreases the carrier mobility, and the ratio m_h^*/m_e^* prescribes the ratio of the electron and hole mobility. The calculated band gap energies and carrier effective masses demonstrate excellent agreement with similar reported values compiled in Table 3, supporting the reliability of the present computational approach. Using the GGA–PBE functional, the computed band gaps and charge-carrier effective masses for A_2AgIrF_6 (A = Cs, Rb, and K) closely match the values documented by Yu *et al.*[57] This consistency reinforces the reliability, significance, and overall scientific validity of the materials under investigation.

For a clearer understanding of bonding in the compounds, the partial density of states (PDOS) and total density of states (TDOS) are shown in Fig. 6, calculated using the TB-mBJ potential. DOS evaluation shows how individual atoms and orbitals of A_2AgIrF_6 (A = Cs, Rb, and K) provide insights into the interaction among atoms, bonding types, and alterations to the material's physical properties.

For Cs_2AgIrF_6, the states close to E_F consist mainly of Ir 5d and Ag 4d states and F 2p states below E_F. The Cs 5s states contribute little and are primarily situated at higher energy levels. The conduction band is mainly formed by the Ir 5d states, while the F 2p states contribute minimally to the conduction band. Likewise, for Rb_2AgIrF_6 and K_2AgIrF_6, the valence band primarily consists of the Ag 4d and Ir 5d states, while the conduction band primarily comprises the Ir 5d state. The VBM is dominated by the Ag 4d, Ir 5d, and F 2p states in all three compounds. The conduction band mainly originates from the Ir 5d orbitals, demonstrating that the Ir 5d states largely determine the electronic structure of the materials.

3.4. Charge density

As pointed out in the analysis of the A_2AgIrF_6 (A = Cs, Rb, and K) compounds, electronic charge density contour plots provide precise descriptions of bond characteristics shown in Fig. 7. The bonding properties and charge transfer are further enhanced using the TB-mBJ method for charge density derived from a converged wave function.[58,59] The samples of A_2AgIrF_6 contain covalent, ionic, and metallic bonding, which define the distribution of the charge density of the compounds in the crystal lattice. These materials comprise AgF_6/IrF_6 connected by corner-sharing octahedra and A^+ cations (Cs^+, Rb^+, and K^+) in the interstitial sites. The high electronegativity difference between A^+ cations and F^- anions allows the structural framework to be controlled by the ions' charges; the electrostatic

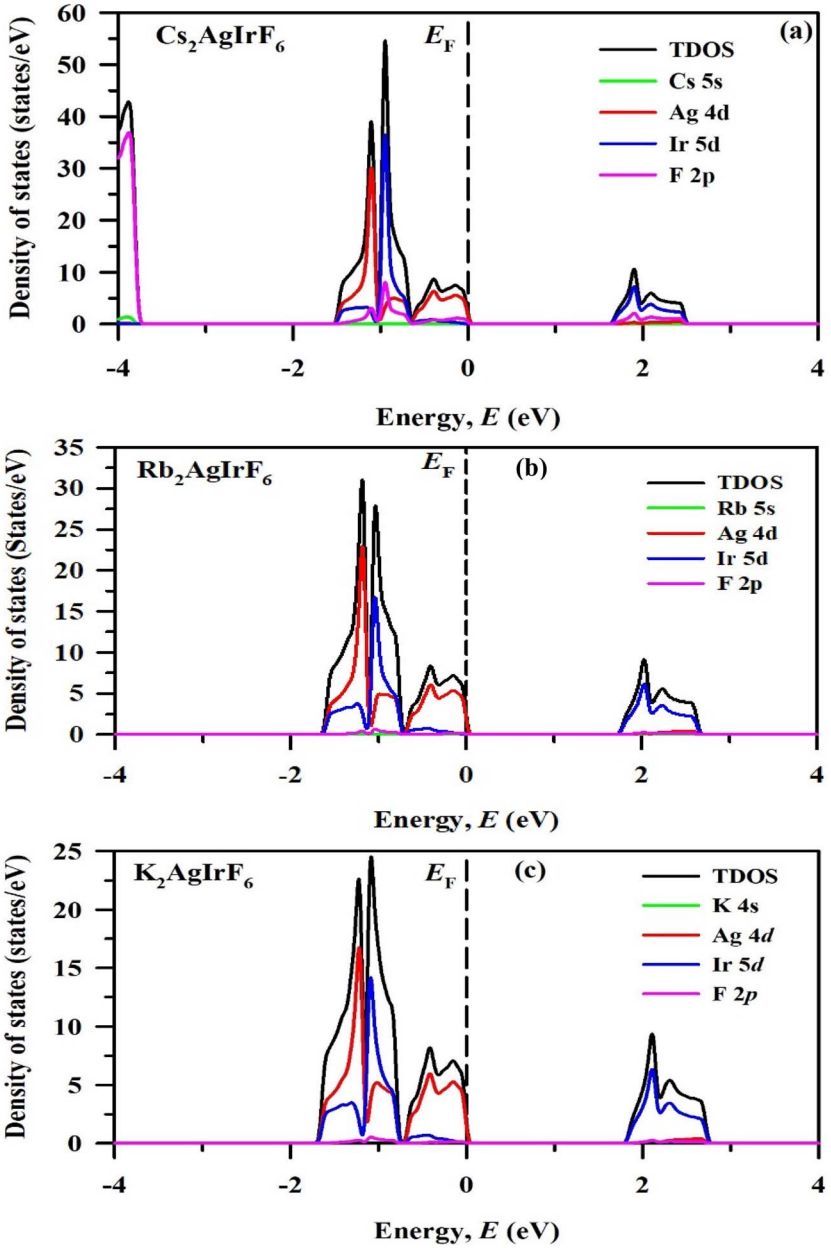

Fig. 6 Total and partial density of states of the (a) Cs_2AgIrF_6, (b) Rb_2AgIrF_6, and (c) K_2AgIrF_6 compounds.

network derived from the ionic bonding proves to be highly stable. Within the AgF_6 and IrF_6 octahedra, the Ag–F and Ir–F bonds exhibit mixed ionic and covalent characteristics. This is attributed to the overlap of Ag/Ir-d-orbitals with F-p-orbitals, leading to enhanced electronic coupling. The high electronegativity of fluorine polarizes the charge density, resulting in localized high-density regions around the F^- ions and along the Ag–F and Ir–F bond axes. Furthermore, the positive charge of the Ag^+ and Ir^{3+} ions leads to semi-delocalized electron contacts, which give rise to the formation of metallic bonds. This delocalization results in intermediate charge density in the Ag–Ir regions, affecting the electrical properties, conductivity, and charge transport. Similar results have been reported in ref. 42, 60 and 61. The intricate balance of charge density, highly localized around F^- ions, intermediate along Ag–F and Ir–F bonds and delocalized between Ag and Ir, defines the electronic behavior of A_2AgIrF_6, making these compounds promising candidates for optoelectronic applications.

3.5. Optical properties

The optical properties of a material are crucial for optoelectronic and photovoltaic devices since they indicate how the material absorbs visible light energy and the internal electric polarization of the available material. In the present work, the dispersive data, such as dielectric function, refractive index $n(\omega)$, extinction coefficient $K(\omega)$, absorption coefficient $\alpha(\omega)$,

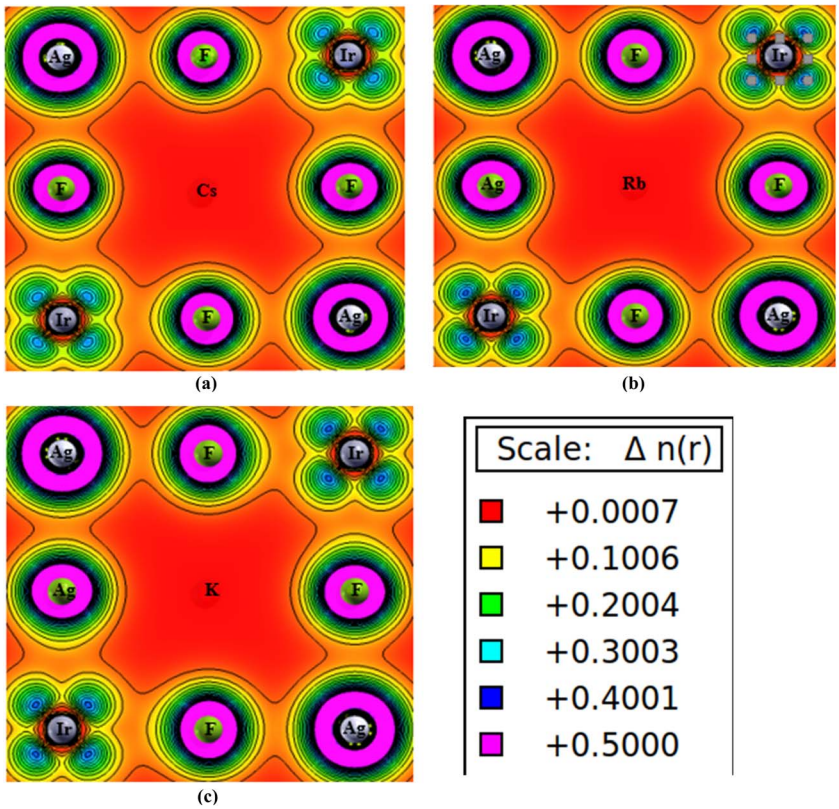

Fig. 7 Charge density of the (a) Cs_2AgIrF_6, (b) Rb_2AgIrF_6, and (c) K_2AgIrF_6 compounds.

conductivity, reflectivity $R(\omega)$, and loss function $L(\omega)$, are computed for these materials. An analysis of the studied photon types shows that ultraviolet photons exhibit higher transmission efficiency through the material compared to infrared or visible photons. Within the visible spectrum, the material demonstrates optical characteristics analogous to metallic behavior, consistent with our initial assumption that all atomic outer shells participate in metallic bond formation. These optical parameters are fully described by the dielectric function $\varepsilon(\omega) = \varepsilon_1(\omega)+i\varepsilon_2(\omega)$, where ε_1 and ε_2 denote the real and imaginary components of the dielectric function, respectively. The real part of the susceptibility, $\varepsilon_1(\omega)$, characterizes the material's response to a field. It can, in turn, be calculated using the Kramers–Kronig relation:[62]

$$\varepsilon_1(\omega) = 1 + \frac{2}{\pi} M \int_0^{\infty} \frac{\varepsilon_2\left(\omega'\right)\omega'}{\omega'^2 - \omega^2} \mathrm{d}\omega, \tag{7}$$

where M stands for a unique integral value attached to the principal component. The absorption of light by a material matches the values of the imaginary dielectric function. Light can transfer electrons from the occupied to unoccupied states of momentum when it travels through any material substance. We can determine $\varepsilon_2(\omega)$ by the momentum matrix of electronic transitions:[63]

$$\varepsilon_2(\omega) = \frac{Ve^2}{2\pi\hbar m^2\omega^2} \int \mathrm{d}^3k \sum_{nn'} \left|\left|kn|p|kn'\right|\right|^2 f(kn) \times \Big(1 - f\left(kn'\right)\Big)\delta(E_{kn} - E_{kn'} - \hbar\omega), \tag{8}$$

where 'e' represents the electric charge, V represents the unit cell volume, $\hbar$ represents the Plank's constant, and $|kn|p|kn'|$ is the momentum transition matrix. Moreover, k represents the wave vector of the conduction band (CB), while kn indicates the valence band (VB) wave vector.

Using the dielectric constants of all the compounds and the equations given below,[64] we can find the refractive index $n(\omega)$, extinction coefficient $k(\omega)$, absorption coefficient $\alpha(\omega)$, conductivity $\sigma(\omega)$, reflectivity $R(\omega)$, and loss function $L(\omega)$. These are all important optical constants:

$$n(\omega) = \left[\frac{\varepsilon_1(\omega)}{2} + \frac{\sqrt{\varepsilon_1{}^2(\omega) + \varepsilon_2{}^2(\omega)}}{2}\right]^{1/2}, \tag{9}$$

$$k(\omega) = \left[-\frac{\varepsilon_1(\omega)}{2} + \frac{\sqrt{\varepsilon_1{}^2(\omega) + \varepsilon_2{}^2(\omega)}}{2}\right]^{1/2}, \tag{10}$$

$$\alpha(\omega) = \sqrt{2}\omega\left[\sqrt{\varepsilon_1{}^2(\omega) + \varepsilon_2{}^2(\omega)} - \varepsilon_1(\omega)\right]^{1/2}, \tag{11}$$

$$\sigma(\omega) = \frac{4\varepsilon_0 E}{e}\varepsilon_2(\omega), \tag{12}$$

$$R(\omega) = \frac{n + ik - 1}{n + ik + 1} \tag{13}$$

and

$$L(\omega) = \frac{\varepsilon_2(\omega)}{\varepsilon_1{}^2(\omega) + \varepsilon_2{}^2(\omega)}. \tag{14}$$

The optical properties of all A_2AgIrF_6 (A = Cs, Rb, and K) compounds have been established and described by photon energies in the range of 0 to 5 eV. According to the real and imaginary parts of the presented materials, the dielectric constant is entirely analogous to the nature of the electronic structure within the visible spectrum range. The numerical values of the real part of the dielectric function of the double perovskite are plotted in Fig. 8(a). For $\varepsilon_1(\omega) > 0$, photons can pass through the material.[65–67] The materials with higher dielectric constants tend to have lower exciton binding energy, which suits their application in solar cells.[68] The computed values of the static dielectric function $\varepsilon_1(0)$ are 3.77, 3.52, and 3.44 for Cs_2AgIrF_6, Rb_2AgIrF_6, and K_2AgIrF_6, respectively, which are higher than those of X_2AuYZ_6 (X = Cs, Rb; Z = Cl, Br, I).[60] The energy of the incident radiation is the main cause of polarization. To obtain desired characteristics in semiconductors, it is important to enhance the polarization values shown in Fig. 8(a), as epitomized by the magnitude of $\varepsilon_1(\omega)$. In the visible light range, the $\varepsilon_1(\omega)$ gradually increases with an increase in the incident radiation up to the polarization peak of 10.28, 10.15, and 10.19 at energies of 1.86, 2.00, and 2.05 eV, respectively. The negative values of A_2AgIrF_6 are in the range of 2.14–3.63 eV. Thus, the three materials exhibit metallic characteristics for the energy ranges and can engage in strong reflection that cannot transmit photons. The calculated graphs for the imaginary part ($\varepsilon_2(\omega)$) of the dielectric function are presented in Fig. 8(b). $\varepsilon_2(\omega)$ is linked to the light absorption characteristics of the materials. The absorption begins at 1.55, 1.63, and 1.72 eV for Cs_2AgIrF_6, Rb_2AgIrF_6, and K_2AgIrF_6, respectively. This energy is similar to the fundamental gap when the system has acquired thermal equilibrium. They rise gradually, and the highest intensities in the visible region are at wavelengths of 11.42, 11.49, and 11.59 for Cs_2AgIrF_6, Rb_2AgIrF_6, and K_2AgIrF_6, respectively. The rates of the peak values represent the electron transfer from the valence band towards the conduction band. This is mainly attributed to a transfer between the Cs, Rb, and K atoms in A and the Ag, Ir, and F atoms in the valence band and the Ir and F atoms in the conduction band of A_2AgIrF_6.

The refractive index $n(\omega)$ determines the probabilities of photon absorption and the speed of light in the material. In the case of solid media, another parameter useful for the comprehension of light transmission and interaction is $n + ik$. It may be helpful for optoelectronics.[69] As the energy of the incident photon increases, the $k(\omega)$ increases and is equal to 0 within the energy band gap. In the region of interband transitions, the $k(\omega)$ changes correspondingly. In this study, we only calculated the real part of the complex refractive index. Representative plots of the refractive index values are plotted as per the calculation

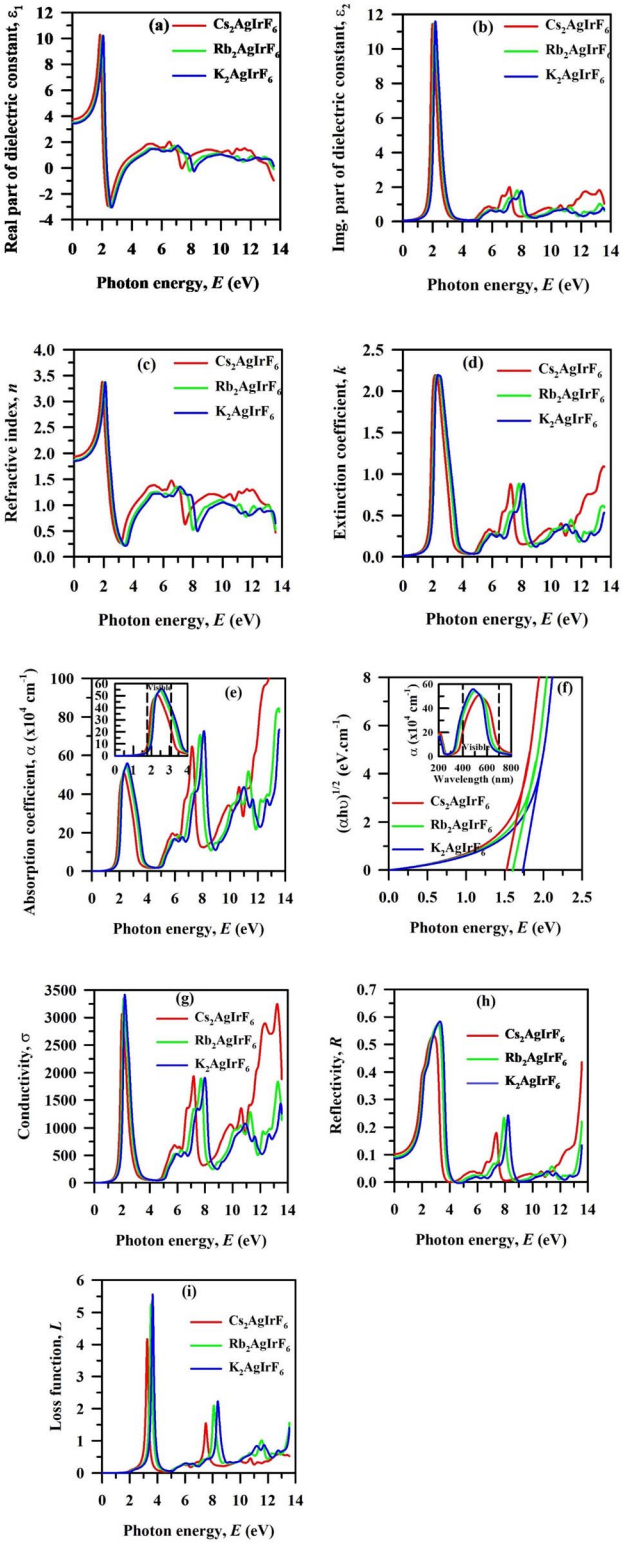

Fig. 8 Optical properties of the A_2AgIrF_6 (A = Cs, Rb, and K) compounds.

Table 4 Computed zero-frequency parameters for the A_2AgIrF_6 (A = Cs, Rb, and K) DHP compounds: real part of the dielectric constant $\varepsilon_1(0)$, static refractive index $n(0)$, reflectivity $R(0)$ and optical band gap using a Tauc plot

DHP	$\varepsilon_1(0)$	$n(0)$	$R(0)$	Optical band gap (eV)
Cs_2AgIrF_6	3.77	1.94	0.10	1.52
Rb_2AgIrF_6	3.52	1.88	0.09	1.61
K_2AgIrF_6	3.44	1.85	0.09	1.75

shown in Fig. 8(c). The specified dependencies $n(\omega) = \varepsilon_r(\omega)$ were positively correlated, confirming that the real part of the dielectric function correlates with the refractive index.[44]

Table 4 presents the zero-frequency optical parameters of A_2AgIrF_6 (A = Cs, Rb, and K). The calculated static refractive indices $n(0)$ range from 1.85 to 1.94, consistent with values typical of semiconducting halide perovskites. The frequency-dependent refractive index $n(\omega)$ varies between 2.0 and 4.0, reflecting the degree of electronic polarizability and the strength of light–matter interaction within the compounds.[70] The peak values of $n(\omega)$ are 3.50 at 1.95 eV for Cs_2AgIrF_6, 3.48 at 2.00 eV for Rb_2AgIrF_6, and 3.46 at 2.05 eV for K_2AgIrF_6. These peaks indicate strong optical dispersion associated with inter-band transitions between the valence and conduction bands. Such refractive index values are appropriate for optoelectronic and photonic materials, as high-quality optical media typically exhibit $n(\omega)$ values between 2.5 and 3.5.[69] The slightly decreasing trend in $n(\omega)$ from Cs to K correlates with the increasing optical band gap, consistent with the inverse relationship between the refractive index and band gap energy, as described by the Penn model. Hence, as the band gap widens, the electronic polarizability decreases, leading to a lower refractive index. This behavior suggests that A_2AgIrF_6 (A = Cs, Rb, and K) compounds possess tunable optical responses, making them suitable candidates for photovoltaic, light-emitting, and photonic applications. The extinction coefficient $k(\omega)$ consistently mirrors the pattern of $\varepsilon_2(\omega)$ and $\alpha(\omega)$, signifying the identification of electromagnetic wave attenuation in the materials, as depicted in Fig. 8(d). The correlation between $k(\omega)$ and $\alpha(\omega)$ is expressed as $k = \frac{\alpha\lambda}{4\pi}$.

Optoelectronic and photovoltaic devices are related to light absorption because the generation and carrier transport processes are proportional to the absorption coefficient $\alpha(\omega)$.[71] Semiconductor absorption coefficients follow those of photons, which determine the basic properties of solar cells. These molecules absorb light more efficiently, leading to better device performance. As shown in Fig. 8(e), the A_2AgIrF_6 (A = Cs, Rb, and K) absorption spectra display strong transitions in the visible region. The characteristic peaks are at 2.96, 3.00 and 3.03 eV for Cs_2AgIrF_6, Rb_2AgIrF_6, and K_2AgIrF_6, respectively. The positions of these peaks are located in the visible range, confirming potential applications for photovoltaic and photodetector devices based on these double halide perovskites. The static peak values are listed in Table 4. The absorption coefficients of the three highest peaks are estimated to be approximately 5.1×10^5 cm^{-1}, 5.4×10^5 cm^{-1}, and 5.5×10^5 cm^{-1} for Cs_2AgIrF_6, Rb_2AgIrF_6, and K_2AgIrF_6, respectively. The studied compounds show higher absorption coefficients than other halide perovskites, including Cs_2AuMF_6 (M = As and Sb),[50] X_2AuYZ_6 (X = Cs and Rb; Z = Cl, Br, and I),[72] A_2AuScX_6 (A = Cs and Rb; X = Cl, Br, and I),[42] and Cs_2AgBiX_6 (X = Cl, Br, and I).[73] The strong absorption coefficients ($\sim 10^5$ cm^{-1}) and suitable optical band gaps (1.52–1.75 eV) indicate that A_2AgIrF_6 (A = Cs, Rb, and K) compounds can serve as efficient absorbing layers in optoelectronic and photovoltaic devices. Materials with absorption coefficients above 10^4 cm^{-1} are generally capable of absorbing most incident visible light within a few hundred nanometers, which reduces material thickness requirements for solar absorbers.[74]

Fig. 8(f) shows that the A_2AgIrF_6 (A = Cs, Rb, and K) compounds exhibit peak absorption at 532, 503, and 482 nm, respectively. These wavelengths exist in the visible light region (400–700 nm), so the compounds can strongly absorb visible light. The optical band gap of the present double halide perovskites was calculated using Tauc plots based on their absorption coefficient spectra.[75] An accurate value of the bandgap is important for developing reliable information about semiconductor properties, and applying the Tauc plot in the wrong way can cause an incorrect estimation of band gap values.[76] The absorption behavior follows the Tauc relation, $(\alpha h\nu)^{1/\eta} = A(h\nu - E_g)$, where α is the absorption coefficient, h is Planck's constant, ν is the photon frequency, A is a material-specific constant, E_g is the optical band gap, and η depends on the band gap type (1/2 for direct and 2 for indirect).[75] Using the TB-mBJ functional, the optical band gaps of A_2AgIrF_6 (A = Cs, Rb, and K) are calculated to be 1.52 eV, 1.61 eV, and 1.75 eV, respectively (Fig. 8(f)), consistent with the electrical band gaps reported in Fig. 5 and Table 3. Furthermore, the calculated optical band gaps are smaller than those reported for related optical materials, such as $BaVO(IO_3)_5$, $BaNbO(IO_3)_5$, and $BaTaO(IO_3)_5$ (2.9–4.2 eV).[77] The comparatively narrower band gaps of A_2AgIrF_6 suggest enhanced absorption in the visible region of the solar spectrum. Consequently, these compounds may be more suitable for visible-light-driven optoelectronic and photovoltaic applications.

Optical conductivity determines the electron transport in a compound under illumination by specific photon energies. For optoelectronic applications, optical conductivity arising from interband electron transitions should fall within the visible range of 1.4–4.0 eV.[70] Substituting different alkali metals has little effect on conductivity. The main conductivity peaks for Cs_2AgIrF_6, Rb_2AgIrF_6, and K_2AgIrF_6 are observed at 2.00 eV (3073 Ω^{-1} cm^{-1}), 2.11 eV (3348 Ω^{-1} cm^{-1}), and 2.19 eV (3416 Ω^{-1} cm^{-1}), respectively (Fig. 8(g)). These peaks, mainly contributed by Ir 5d states, are key to the electronic structure and confirm the high optical conductivity of the compounds within the visible spectrum.

The reflectivity spectra $R(\omega)$ of the A_2AgIrF_6 (A = Cs, Rb, and K) double halide perovskite compounds are presented in Fig. 8(h), and these systems exhibit different reflectivity behaviors over the whole photon energy range. The static

reflectivity values for these materials are as follows: 10% for Cs_2AgIrF_6, 9% for Rb_2AgIrF_6, and 9% for K_2AgIrF_6. The low $R(\omega)$ values in the energy range of 0 to the band gap confirm its light trapping ability; thus, they are suitable for optoelectronics and photovoltaic applications. The reflectivity rises steeply towards the absorption edge region, and the peak is observed at a higher energy region, which may be attributed to the interband transitions. This behavior is quite typical for materials with pronounced photon-matter coupling. The low reflectivity in the visible spectrum also supports the applicability of these compounds in light-harvesting technologies, as the compounds limit reflection while enhancing absorption capability. The energy loss function, shown in Fig. 8(i), illustrates the energy lost by electrons as they propagate through the material. Prominent peaks are observed at approximately 3.25 eV for Cs_2AgIrF_6, 3.52 eV for Rb_2AgIr_6, and 3.66 eV for K_2AgIrF_6, indicating significant electron scattering at these energies, which aligns with their optical conductivity behavior. Compounds with low reflectivity and reduced energy loss are ideal candidates for solar cell absorber layers. Owing to their adjustable band gaps, high dielectric strength, excellent absorbance, and efficient photoconductivity, such compounds are highly promising for optoelectronic and solar cell device applications.

3.6. Mechanical properties

The mechanical properties of a crystal are principally governed by its elastic constants, which determine the reaction of the crystal to loads. It is important to acquire such information in studies concerned with the mechanical behavior of materials. In this work, the mechanical properties and the marks related to the elasticity use deformability coefficients, C_{11}, C_{12} and C_{44}, for different compounds. The mechanical stability of the perovskite compounds was evaluated using the following criteria: $C_{11} - C_{12} > 0$, $C_{44} > 0$, and $C_{11} + 2C_{12} > 0$.[78] Strength, another first-order texture property that provides some insight into the nature of a material, was also considered. The individual elastic coefficients of the studied compounds are reported in Table 5.

Specific mechanical properties of A_2AgIrF_6 (A = Cs, Rb, and K) were predicted, which include bulk modulus (B), Pugh's ratio (B/G), Young's modulus (Y), shear modulus (G), and Poisson's ratio (ν). The bulk modulus (B) is the measure of the stiffness of a material with respect to changes in its volume when pressure is applied. Shear modulus (G) refers to the ratio of the applied shear stress to the resulting shear strain. From the ratio of stress to strain at uniaxial deformation, Young's modulus (Y) was deduced as an indicator of the elasticity of the material. The formulas used for these calculations are as follows:[79–81]

$$B = \frac{C_{11} + 2C_{12}}{3}, \tag{15}$$

$$G = \frac{3C_{44} + C_{11} - C_{12}}{5}, \tag{16}$$

$$Y = \frac{9BG}{3B + G} \tag{17}$$

and

$$\nu = \frac{3B - Y}{2(3B + G)}. \tag{18}$$

In A_2AgIrF_6, the C_{11} (mechanical linear stiffness) is larger than C_{12} and C_{44}, which suggests that the materials are more durable when pressure is applied. The compounds, therefore, stand in the order of Rb_2AgIrF_6, which has the highest C_{11} (162.82 GPa) and, thus, the best B of 75.05 GPa because the higher C_{11} means a higher resistance to volumetric compression. Shear modulus (G) is also closely related to the anti-deformation of the shape, and it is, therefore, profound in Rb_2AgIrF_6 with 28.90 GPa, meaning that a greater force is needed to afford the compound this shape than Cs_2AgIrF_6 or K_2AgIrF_6.

The tensile elastic modulus Y, which predicts the stiffness of a material under tension or compression, is higher in Rb_2AgIrF_6, with values of up to 76.84 GPa. From the results above, it can be inferred that the B/G ratio is greater than 1.75 for all the compounds under study, indicating their ductility.[82] However, for the three compounds, K_2AgIrF_6 has the highest B/G ratio (2.90) and is, therefore, more ductile than the other two compounds. High ductility and room temperature stability make these compounds useful in flexible applications, such as the thin film absorber layers of foldable electronics and biomedical devices.[83,84] Poisson's ratio (ν) is the other mechanical property of concern, which represents the lateral contraction per unit length when the material is subjected to axial loads, which is a measure of flexibility.[85] The lattice flexible character of the compounds can be estimated using the value of ν, which is higher than 0.26 for all target compounds, whereas K_2AgIrF_6 has the highest value of $\nu = 0.35$. Thus, their capability of stress engineering is demonstrated, and the band gap can be tuned by controlled stress. Non-zero positive values of reported Cauchy pressure (CP) values for the compounds suggest the existence of ionic bonding between the atoms.[86] Moreover, the values of elastic anisotropy coefficients (A), which are determined from the relationship[87] $A = \frac{2C_{44}}{3C_{11} - C_{12}}$ are not equal to 1, which confirms the anisotropic nature. Of all the compounds,

Table 5 Mechanical properties of the A_2AgIrF_6 (A = Cs, Rb, and K) compounds

Parameters	Cs_2AgIrF_6	Rb_2AgIrF_6	K_2AgIrF_6
C_{11} (GPa)	127.79	162.82	162.67
C_{12} (Gpa)	35.70	31.17	28.21
C_{44} (Gpa)	16.22	15.42	11.14
B (Gpa)	66.39	75.05	73.03
G (Gpa)	25.02	28.90	25.15
Y (Gpa)	66.69	76.84	67.67
B/G	2.65	2.60	2.90
ν	0.33	0.33	0.35
C_P	19.48	15.75	17.07
A	0.35	0.23	0.17

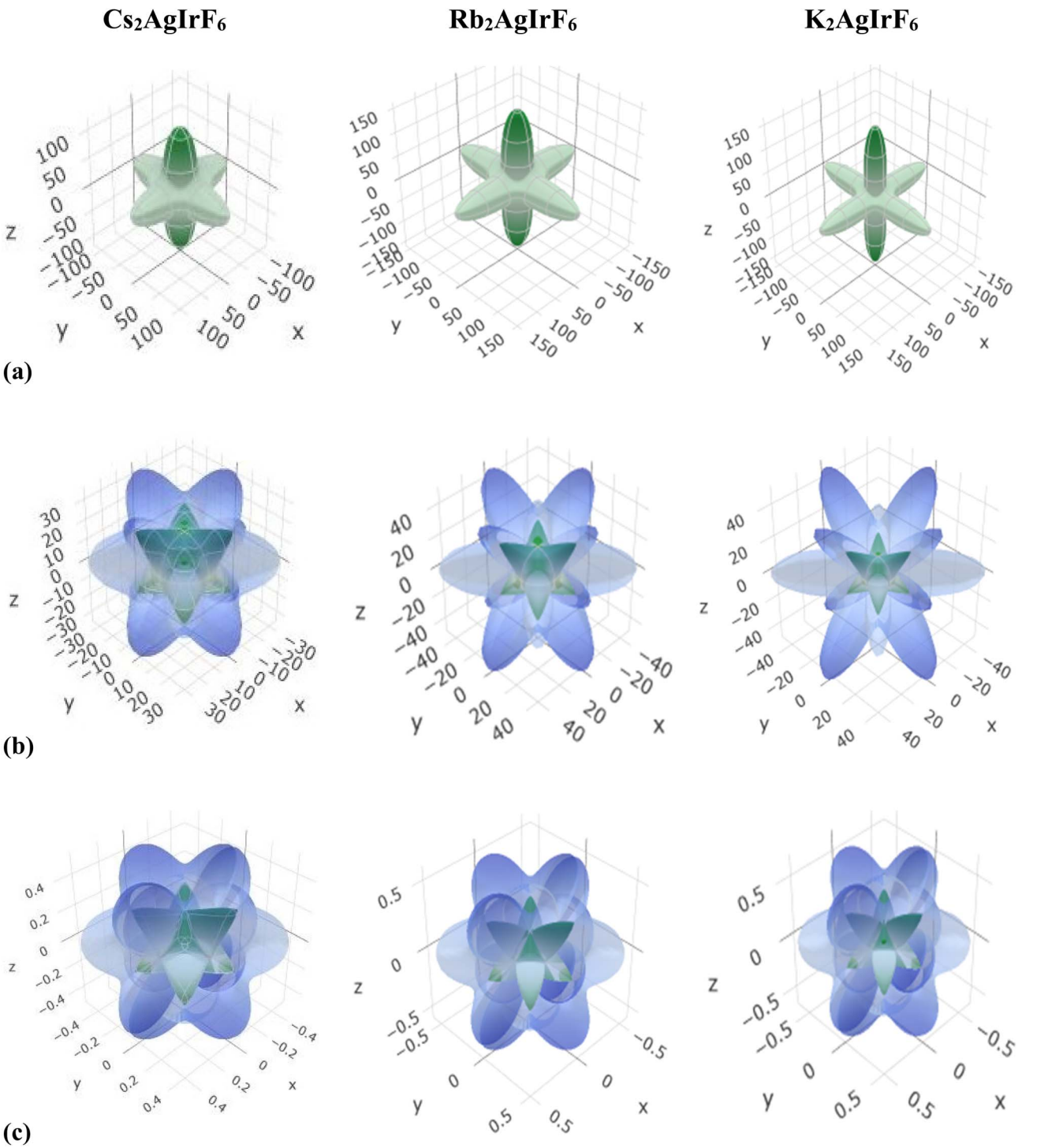

Fig. 9 3-D representations of the (a) Young's modulus, (b) shear modulus, and (c) Poisson's ratio for the A_2AgIrF_6 (A = Cs, Rb, and K) compounds.

Cs_2AgIrF_6 has the highest *A* value of 0.35, indicating that it is more directional. These outcomes hint at the anisotropic character of the researched compounds and their high potential for use in modern technologies as materials with desired mechanical and structural properties. The anisotropic mechanical response of the A_2AgIrF_6 lead-free double perovskites was examined using elastic constants obtained from first-principles calculations, analyzed through the ELATE elastic tensor visualization tool.[88] Three-dimensional orientation-dependent plots of Young's modulus, shear modulus, and Poisson's ratio are illustrated in Fig. 9(a–c). In such a diagram, the degree of anisotropy is shown with different colored contours, and its sharpness is in proportion to the amount of curvature. A larger curvature of the contours inward to the

Table 6 Minimal and maximal values of the elastic modulus and elastic anisotropy of the A_2AgIrF_6 (A = Cs, Rb, and K) compounds

	Young's modulus (GPa)		Linear compressibility (TPa^{-1})		Shear modulus (GPa)		Poisson's ratio	
HDPs	Y_{min}	Y_{max}	β_{min}	β_{max}	G_{min}	G_{max}	ν_{min}	ν_{max}
Cs_2AgIrF_6	44.99	112.20	5.02	5.02	16.22	46.05	0.10	0.63
Rb_2AgIrF_6	43.29	152.80	4.44	4.44	15.42	65.82	0.05	0.71
K_2AgIrF_6	31.80	154.33	4.56	4.56	11.14	67.23	0.04	0.78
Elastic anisotropy A_x								
	A_Y		A_β		A_G		A_ν	
Cs_2AgIrF_6	2.49		1.00		2.84		6.13	
Rb_2AgIrF_6	3.53		1.00		4.27		12.81	
K_2AgIrF_6	4.85		1.00		6.03		20.55	

sphere center is associated with a stronger anisotropy, and a nearly circular outline corresponds to weaker anisotropy.[89] As calculated from the spatial dependence maps, shear modulus and Poisson's ratio exhibit a strong directionality, consistent with the computed anisotropy factor that confirms the studied compounds to be anisotropic (Table 6).

3.7. Thermodynamic properties

The Debye temperature (θ_D) is a fundamental thermodynamic parameter that governs the thermal properties and heat capacity of solids across different temperature ranges. It serves as an indicator of how material properties evolve with temperature variation. Several theoretical approaches have been formulated to evaluate θ_D, most of which incorporate the mean sound velocity (v_m) as a critical factor in describing lattice vibrations and thermal response. The Debye temperature can be determined using the following equation:[90]

$$\theta_D = \frac{h}{k_B}\left[\frac{3n}{4\pi}\left(\frac{N_A\rho}{M}\right)\right]^{\frac{1}{3}} v_m, \quad (19)$$

where $\hbar$ is the normalized Planck's constant, k_B is Boltzmann's constant, n represents the number of atoms, V is the unit-cell volume, and v_m denotes the average acoustic velocity. The latter is derived from the following relation:[90]

$$v_m = \left[\frac{1}{3}\left(\frac{2}{v_t^3} + \frac{1}{v_l^3}\right)\right]^{-\frac{1}{3}}, \quad (20)$$

where v_t and v_l denote the transverse and longitudinal sound velocities, respectively. The shear modulus (G), bulk modulus (B), and density (ρ) are used to obtain these additional parameters as follows:[90]

$$v_l = \sqrt{(3B + 4G)/3\rho} \quad (21)$$

and

$$v_t = \sqrt{G/\rho}. \quad (22)$$

In the presented data, θ_D increases progressively from 253.34 K (Cs_2AgIrF_6) to 291.25 K (Rb_2AgIrF_6) and 296.09 K (K_2AgIrF_6), which correlates with the increase in sound velocities (v_l, v_t, and v_m) and the decrease in density. The Debye temperature increases by ~15–17% as Cs is replaced by Rb and K. This rise reflects the influence of the smaller ionic radii of Rb^+ and K^+, which cause lattice contraction and stronger interatomic bonding. A denser bond network enhances the average sound velocity (v_m) and, therefore, increases θ_D. The increase in θ_D signifies that the lattice of K_2AgIrF_6 is stiffer and vibrates at higher frequencies compared to Cs_2AgIrF_6. This improvement in vibrational energy correlates with better thermal stability, stronger bonding strength, and higher thermal conductivity potential.

One of the big challenges in fabricating solar cells is to identify materials that can withstand extreme heat during manufacturing without breaking down or without driving costs too high. Low-melting-point materials run the risk of melting or cracking, forming defects, while very high-melting-point materials are expensive and hard to work with.[91] The melting behavior is commonly described using the elastic constant (C_{11}), which gives the measure of a material's resistance to thermal deformation. The melting temperature (T_m) of the A_2AgIrF_6 materials was calculated using the empirical formula reported by Fine *et al.*:[92]

$$T_m\,(K) = 553 + (5.911)C_{11}. \quad (23)$$

The obtained melting temperatures suggest that the investigated double perovskites are thermodynamically stable and can be synthesized under ambient conditions. Among them,

Table 7 Calculated crystal density ρ (gm cm^{-3}), longitudinal, transverse, and average sound velocities (v_l, v_t and v_m) (m s^{-1}), Debye temperature $\Theta_D(K)$, and melting temperature $T_m(K)$ for the A_2AgIrF_6 (A = Cs, Rb, and K) compounds

Compounds	ρ	v_l	v_t	v_m	Θ_D	T_m
Cs_2AgIrF_6	6.45	3932.91	1969.72	2209.44	253.34	1308.25
Rb_2AgIrF_6	5.80	4425.28	2232.25	2502.86	291.25	1514.40
K_2AgIrF_6	4.99	4639.54	2253.84	2532.51	296.09	1515.28

K_2AgIrF_6 displays a greater melting point than that of Cs_2AgIrF_6 and Rb_2AgIrF_6. A summary of the thermodynamic parameters derived from the elastic constants is presented in Table 7.

The stability of the sample was investigated by phonon mode analysis at various temperatures, enabling the determination of fundamental thermodynamic parameters, such as enthalpy, free energy, and entropy. These quantities are directly related to phonon vibration frequencies, expressed as follows:[47]

$$H(T) = E_{\text{tot}} + \frac{1}{2}\int g(\omega)\hbar\omega \mathrm{d}\omega + \int \frac{\hbar\omega}{e^{\frac{\hbar\omega}{K_B T}} - 1} g(\omega)\mathrm{d}\omega, \quad (24)$$

$$F(T) = E_{\text{tot}} + \frac{1}{2}\int g(\omega)\hbar\omega \mathrm{d}\omega + K_B T \int g(\omega)\ln\left(1 - e^{\frac{\hbar\omega}{K_B T}}\right)\mathrm{d}\omega \quad (25)$$

and

$$S(T) = K_B\left[\int \frac{\frac{\hbar\omega}{K_B T}}{e^{\frac{\hbar\omega}{K_B T}} - 1} g(\omega)\mathrm{d}\omega - \int g(\omega)\ln\left(1 - e^{\frac{\hbar\omega}{K_B T}}\right)\mathrm{d}\omega\right], \quad (26)$$

where $g(\omega)$ denotes the phonon density of states, K_B is the Boltzmann constant, E_{tot} is the minimum total energy, and $\hbar$ represents the normalized Planck constant. The temperature-dependent variations of the enthalpy, free energy, entropy, heat capacity, and Debye temperature for A_2AgIrF_6 (A = Cs, Rb, and K) are illustrated in Fig. 10. The enthalpy of the system exhibits a linear increase with temperature, whereas the free energy decreases following an exponential decay trend, as illustrated in Fig. 10(a). Entropy, which determines the degree of disorder in a material, rises exponentially with an increase in

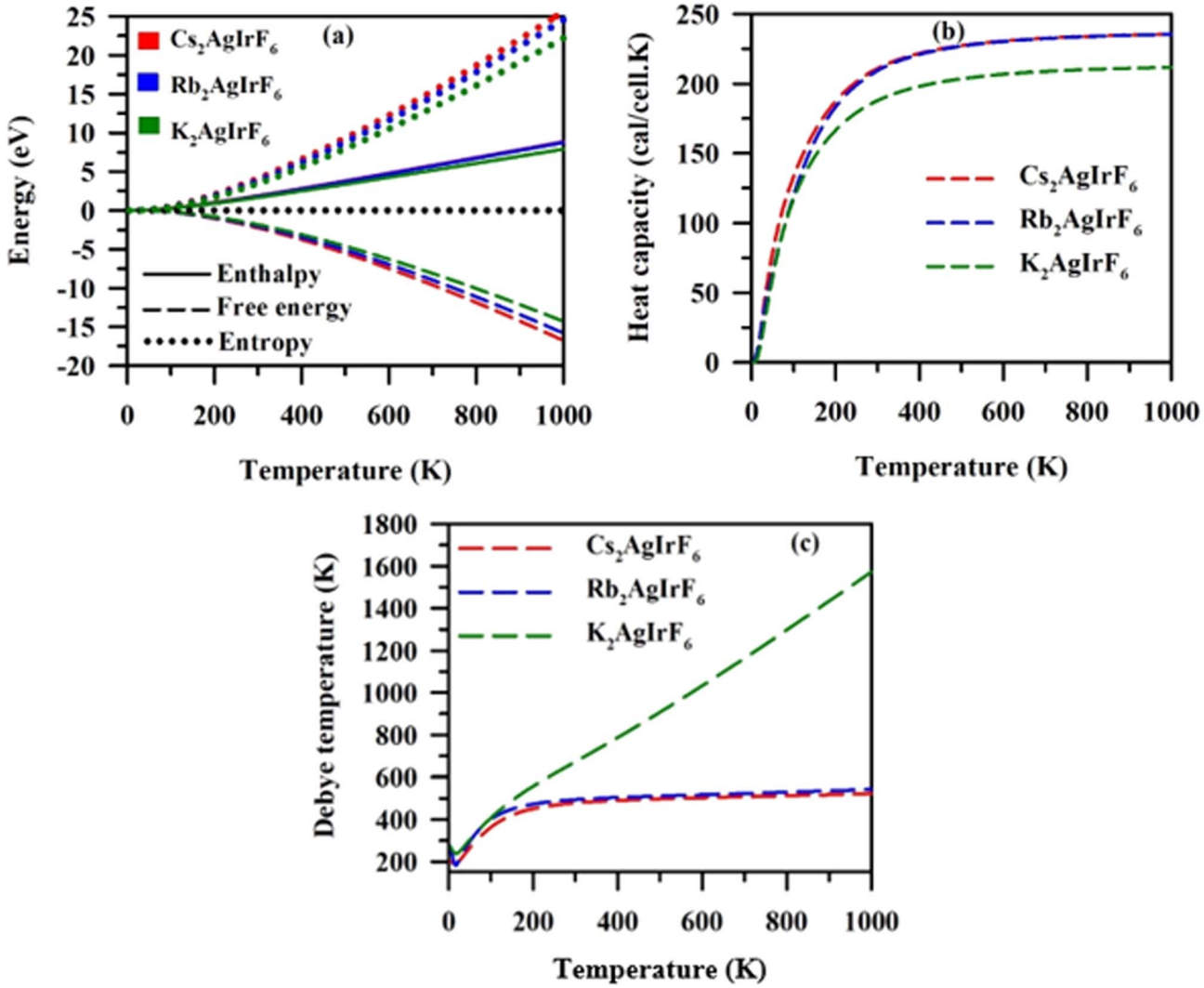

Fig. 10 Thermodynamic properties of the A_2AgIrF_6 (A = Cs, Rb, and K) double perovskite compounds.

temperature. This behavior results from the enhanced thermal motion of atoms at higher temperatures, which increases molecular disorder.[93] Heat capacity, reflecting the material's ability to store thermal energy through contributions from both lattice vibrations and electronic motion, shows a sharp increase between 0 and 200 K, consistent with the Debye model[93] (Fig. 10(b)). At up to 500 K, most low-energy vibrational modes become thermally active. Beyond 500 K, the heat capacity reaches a plateau, with further temperature increases producing negligible change, in accordance with the Dulong–Petit law.[94] The temperature-dependent behavior of the Debye temperature is presented in Fig. 10(c). A clear compositional trend (K → Rb → Cs) is observed in the thermodynamic properties shown in Fig. 10(c). This behavior originates from the systematic variation in the A-site ionic radius (K^+ < Rb^+ < Cs^+), which affects lattice volume, bonding strength, and phonon dynamics. At 0 K, the Debye temperatures for Cs_2AgIrF_6, Rb_2AgIrF_6, and K_2AgIrF_6 are approximately 200.99 K, 266.36 K, and 269.74 K, respectively. This trend agrees with Anderson's formula, since smaller A-site cations reduce the lattice volume and increase the sound velocity, leading to higher Debye temperatures. This is consistent with Anderson's formula of Debye temperature by elastic constants. Under constant pressure, the Debye temperature increases with temperature, reflecting the thermal stiffening of lattice vibrations.

4. Conclusions

In this study, the structural, electronic, optical, mechanical, and thermodynamic properties of lead-free double perovskites A_2AgIrF_6 (A = Cs, Rb, and K) were systematically investigated using density functional theory (DFT). The calculated tolerance factors, formation energies and phonon dispersion curves demonstrate that these compounds are thermodynamically and dynamically stable based on AIMD simulations, further confirming their dynamic stability at room temperature. Electronic structure studies show that the indirect band gaps lie in the range of 1.65–1.83 eV (TB-mBJ), which are well within the optimum photovoltaic window. The small band gap, coupled with low carrier effective masses, are suggestive of efficient charge transport and weak recombination losses; the latter is critical in designing high-performance optoelectronic devices. The optical calculations demonstrate large absorption coefficients (>10^5 cm^{-1}) in the visible region, large dielectric constants, as well as the low reflectivity (<10%) of these materials, indicating their significant light-harvesting capabilities. The *B*/*G* ratios and Poisson's ratio values are all high, which is consistent with the ductile properties and anisotropic mechanical behavior that demonstrate structural flexibility for applications in thin-film or flexible electronics. We also measured the Debye and melting temperatures, which verify high thermal stability and ensure their long-term durability in working status. In summary, A_2AgIrF_6 (A = Cs, Rb, and K) double perovskites appear as earth-abundant, mechanically stable and opto-electronically effective materials. Their stability, visible-light absorption ability and ductility mean that the materials could be useful in future solar cells and energy-harvesting devices that adopt a more environmentally friendly approach than toxic lead-based perovskites for next-generation green-energy technologies. This study will guide the development of lead-free perovskite materials, which can be employed in highly efficient and environmentally safe energy technologies.

Author contributions

M. A. Rayhan: writing – original draft, methodology, conceptualization, formal analysis, data calculations, validation. M. M. Hossain: writing – review & editing, validation. M. M. Uddin: writing – review & editing, validation. M. A. Ali: conceptualization, formal analysis, validation, writing – review & editing, supervision, software.

Conflicts of interest

We declare that we have no competing interests.

Data availability

The relevant data from this study are available from the corresponding author upon reasonable request.

Acknowledgements

This work was carried out with the aid of a grant (grant number 21-378 RG/PHYS/AS_G-FR3240319526) from UNESCO-TWAS and the Swedish International Development Co-operation Agency (SIDA). The views expressed herein do not necessarily represent those of UNESCO-TWAS, SIDA or its Board of Governors.

References

1 M. K. Jana, S. M. Janke, D. J. Dirkes, S. Dovlegeldi, C. Liu, X. X. Qin, K. Gongogdu, W. You, V. Blum and D. B. Mitzi, *J. Am. Chem. Soc.*, 2019, **141**, 7955–7964.
2 J. Yang, P. Zhang and S.-H. Wei, *J. Phys. Chem. Lett.*, 2018, **9**, 31–35.
3 Z. Xiao, K. Z. Du, W. Meng, J. Wang, D. B. Mitzi and Y. Yan, *J. Am. Chem. Soc.*, 2017, **139**, 6054–6057.
4 K. C. Bhamu, A. Soni and J. Sahariya, *Sol. Energy*, 2018, **162**, 336–343.
5 S. Ameen, M. A. Rub, S. A. Kosa, K. A. Alamry, M. S. Akhtar, H. S. Shin, H. K. Seo, A. M. Asiri and M. K. Nazeeruddin, *ChemSusChem*, 2016, **9**, 10–27.
6 E. Meyer, D. Mutukwa, N. Zingwe and R. Taziwa, *Metals*, 2018, **8**, 667.
7 W. Nie, H. Tsai, R. Asadpour, J. C. Blancon, A. J. Neukirch, G. Gupta, J. J. Crochet, M. Chhowalla, S. Tretiak, M. A. Alam and H. L. Wang, *Science*, 2015, **347**, 522–525.
8 N. Das, *Nanostructured Solar Cells, BoD-Books on Demand*, 2017.
9 I. E. Yahiaoui, A. Lazreg, Z. Dridi, Y. Al-Douri and B. Bouhafs, *Bull. Mater. Sci.*, 2018, **41**, 1–5.

10 M. H. Benkabou, M. Harmel, A. Haddou, A. Yakoubi, N. Baki, R. Ahmed, Y. Al-Douri, S. V. Syrotyuk, H. Khachai, R. Khenata and C. H. Voon, *Chinese J. Phys.*, 2018, **56**, 131–144.
11 L. Hasni, M. Ameri, D. Bensaid, I. Ameri, S. Mesbah, Y. Al-Douri and J. Coutinho, *J. Supercond. Nov. Magn.*, 2017, **30**, 3471–3479.
12 M. Rafique, Y. Shuai, I. Ahmed, R. Shaikh and M. A. Tunio, *Appl. Surf. Sci.*, 2019, **480**, 463–471.
13 M. Rafique, N. H. Mirjat, A. M. Soomro, S. Khokhar and Y. Shuai, *Phys. Lett. A*, 2018, **382**, 1108–1119.
14 R. Muhammad, Y. Shuai and H. P. Tan, *J. Mater. Chem. C*, 2017, **5**, 8112–8127.
15 S. A. Mir and D. C. Gupta, *Int. J. Energy Res.*, 2021, **45**, 14603–14611.
16 M. K. Hossain, A. A. Arnab, D. P. Samajdar, M. H. K. Rubel, M. M. Hossain, M. R. Islam, R. C. Das, H. Bencherif, M. F. Rahman, J. Madan and R. Pandey, *Energy Fuels*, 2023, **37**, 13377–13396.
17 G. H. Kim and D. S. Kim, *Joule*, 2021, **5**, 1033–1035.
18 E. T. McClure, M. R. Ball, W. Windl and P. M. Woodward, *Chem. Mater.*, 2016, **28**, 1348–1354.
19 F. Wei, Z. Deng, S. Sun, N. T. P. hartonto, H. L. Seng, T. Buosassisi, P. D. Bristowe and A. K. Cheetham, *Chem. Commun.*, 2019, **55**, 3721–3724.
20 C. Zhang, L. Gao, S. Teo, Z. Guo, Z. Xu, S. Zhao and T. Ma, *Sustain. energy & fuels*, 2018, **2**, 2419–2428.
21 G. M. Mustafa, S. Saba, Q. Mahmood, N. A. Kattan, N. Sfina, T. Alshahrani, A. Mera, G. A. Mersal and M. A. Amin, *Opt. Quantum Electron.*, 2023, **55**, 527.
22 N. H. Alotaibi, G. M. Mustafa, N. A. Kattan, Q. Mahmood, H. Albalawi, M. Morsi, H. H. Hafez, H. I. Mahmood and M. A. Amin, *J. Solid State Chem.*, 2022, **313**, 123353.
23 M. Saeed, I. U. Haq, A. S. Saleemi, S. U. Rehman, B. U. Haq, A. R. Chaudhry and I. Khan, *J. Phys. Chem. Solids*, 2022, **160**, 110302.
24 M. Babaei, V. Ahmadi and G. Darvish, *J. Phys. Chem. Solids*, 2022, **169**, 110880.
25 R. Anbarasan, M. Srinivasan, R. Suriakarthick, H. Albalawi, J. K. Sundar, P. Ramasamy and Q. Mahmood, *J. Solid State Chem.*, 2022, **310**, 123025.
26 G. Nazir, Q. Mahmood, M. Hasan, M. M. Al-Anazy, N. A. Kattan, N. Sfina, M. A. Amin, A. Mera and H. H. Somaily, *Phys. Scr.*, 2023, **98**, 25811.
27 M. A. Ali, R. A. Alshgari, A. A. Awadh Bahajjaj and M. Sillanpää, *J. Taibah Univ. Sci.*, 2023, **17**, 2170680.
28 M. Zanib, M. W. Iqbal, M. Manzoor, M. Asghar, R. Sharma, N. N. Ahmad, S. M. Wabaidur, M. A. Habila, S. A. Abdelmohsen, A. M. Abdelbacki and I. Sidique, *Mater. Sci. Eng. B*, 2023, **295**, 116604.
29 A. Bhorde, R. Waykar, S. R. Rondiya, S. Nair, G. lonkar, A. Funde and N. Y. Dzade, *ES Mater. & Manuf.*, 2021, **12**, 43–52.
30 A. I. Aljameel, G. M. Mustafa, B. Younas, H. D. Alkhaldi, F. Alharjri, G. I. Ameereh, N. Sfina, A. S. Alshomrany and Q. Mahmood, *J. Phys. Chem. Solids*, 2024, **189**, 111953.
31 S. Al-Qaisi, M. Mushtaq, S. Alomairy, T. V. Vu, H. Rached, B. U. Haq, Q. Mahmood and M. S. Al-Buriahi, *Mater. Sci. Semicond. Process.*, 2022, **150**, 106947.
32 G. M. Mustafa, F. Basheer, N. A. Noor, B. Younas, A. Mahmood, M. Iqbal and F. S. Almubaddel, *ECS J. Solid State Sci. Technol.*, 2023, **12**, 103009.
33 S. Kumari, P. K. Kamlesh, L. Kumari, S. Kumar, S. Kumari, R. Singh, R. Gupta, M. S. Chauhan, U. Rani and A. S. Verma, *J. Mol. Model.*, 2023, **29**, 195.
34 A. Ayyaz, G. Murtaza, M. Umer, A. Usman and H. H. Raza, *J. Mater. Res.*, 2023, **38**, 4609–4624.
35 A. U. Haq, T. S. Ahmad, M. Amin, A. Bakar, A. Afaq, N. Ehsan, S. M. Ramay and A. A. Siddig, *Phys. Scr.*, 2023, **98**, 115972.
36 P. Blaha, K. Schwarz, F. Tran, R. Laskowski, G. K. Madsen and L. D. Marks, *J. Chem. Phys.*, 2020, **152**, 074101.
37 W. Kohn and L. Sham, *Phys. Rev.*, 1965, **140**, A1133.
38 F. Tran and P. Blaha, *Phys. Rev. Lett.*, 2009, **102**, 226401.
39 D. Koller, F. Tran and P. Blaha, *Phys. Rev. B–Condensed Matter Mater. Phys.*, 2012, **85**, 155109.
40 H. J. Monkhorst and J. D. Pack, *Phys. Rev. B*, 1976, **13**, 5188.
41 K. Lv, S. Qi, G. Liu, Y. Lou, J. Chen and Y. Zhao, *Chem. Commun.*, 2019, **55**, 14741–14744.
42 S. Mahmud, M. A. Ali, M. M. Hossain and M. M. Uddin, *Vacuum*, 2024, **221**, 112926.
43 V. M. Goldschmidt, *Naturwissenschaften*, 1926, **14**, 477–485.
44 C. Li, X. Lu, W. Ding, L. Feng, Y. Gao and Z. Guo, *Struct. Sci.*, 2008, **64**, 702–707.
45 C. J. Bartel, C. Sutton, B. R. Goldsmith, R. Ouyang, C. B. Musgrave, L. M. Ghiringhelli and M. Scheffler, *Sci. Adv.*, 2019, **5**, eaav0693.
46 S. A. Mir and D. C. Gupta, *J. Alloys Compd.*, 2021, **854**, 156000.
47 S. Baroni, S. De Gironcoli, A. Dal Corso and P. Giannozzi, *Rev. Mod. Phys.*, 2001, **73**, 515.
48 M. D. Segall, P. J. Lindan, M. A. Probert, C. J. Pickard, P. J. Hasnip, S. J. Clark and M. C. Payne, *J. Phys. Condens. Matter.*, 2002, **14**, 2717–2744.
49 M. Markov, X. Hu, H. C. Liu, N. Liu, S. J. Poon, K. Esfarjani and M. Zebarjadi, *Sci. Rep.*, 2018, **8**, 9876.
50 S. Mahmud, U. Ahmed, M. A. U. Z. Atik, M. M. Hossain, M. M. Uddin and M. A. Ali, *Phys. Chem. Chem. Phys.*, 2025, **27**, 4686–4703.
51 M. S. Parves, M. A. B. Siddique, M. Tarekuzzaman, N. Shahadath, S. Ahmad, M. Rasheduzzaman, M. M. Hossen, Y. Arafat and M. Z. Hasan, *Energy Nexus*, 2025, **20**, 100549.
52 W. Shockley and H. Queisser, *J. Appl. Phys.*, 1961, **32**, 510–519.
53 T. Nakajima and K. Sawada, *J. Phys. Chem. Lett.*, 2017, **8**, 4826–4831.
54 M. S. Parves, S. Mahmud, M. Tarekuzzaman, M. A. Rayhan, M. Rasheduzzaman and M. Z. Hasan, *AIP Adv.*, 2024, **14**, 105034.
55 T. Saha, M. M. H. Babu, M. Arifuzzaman and J. Podder, *Phys. Chem. Chem. Phys.*, 2022, **24**, 26609–26621.
56 N. H. Alotaibi, *J. Phys. Chem. Solids*, 2022, **171**, 110984.
57 J. Wu, J. H. Li and Y. X. Yu, *ChemPhysChem*, 2020, **21**, 2539–2549.

58 R. Hoffmann, *Rev. Mod. Phys.*, 1988, **60**, 601.
59 C. D. Gelatt Jr, A. R. Williams and V. L. Moruzzi, *Phys. Rev. B*, 1983, **27**, 2005.
60 S. Mahmud, M. M. Hossain, M. M. Uddin and M. A. Ali, *J. Phys. Chem. Solids*, 2025, **196**, 112298.
61 M. Wuttig, C. F. Schon, M. Schumacher, J. Robertson, P. Golub, E. Bousquet, C. Gatti and J. Y. Raty, *Adv. Funct. Mater.*, 2022, **32**, 2110166.
62 V. Lucarini, J. J. Saarinen, K. E. Peiponen and E. M. Vartiainen, *Kramers-Kronig Relations in Optical Materials Research*, Springer Science & Business Media, 2005, vol. 110, pp. 27–48.
63 A. Kojima, K. Teshima, Y. Shirai and T. Miyasaka, *J. Am. Chem. Soc.*, 2009, **131**, 6050–6051.
64 S. Mahmud, M. Atik, M. N. Mostakim, M. Tarekuzzaman and M. Z. Hasan, *Comput. Condens. Matter*, 2024, **40**, e00950.
65 G. Ling-Yun, Z. Ping, C. Qian, L. Zhi-Hao, X. Jie and G. Feng, *ACTA Phys. Sin.*, 2021, **70**, 227101.
66 D. Y. Hu, X. H. Zhao, T. Y. Tang, L. Li, L. K. Gao and Y. L. Tang, *Opt. Mater.*, 2021, **119**, 111316.
67 A. Hossain, M. A. Ali, M. M. Uddin, S. H. Naqib and M. M. Hossain, *Mater. Sci. Semicond. Process.*, 2024, **172**, 108092.
68 E. Oyeniyi, *Solid State Commun.*, 2022, **355**, 114927.
69 E. F. Schubert, J. K. Kim and J. Q. Xi, *Phys. Status Solidi*, 2007, **244**, 3002–3008.
70 H. H. Hegazy, G. M. Mustafa, A. Nawaz, N. A. Noor, A. Dahshan and I. Boukhris, *J. Mater. Res. Technol.*, 2022, **19**, 1271–1281.
71 R. Yang, D. Li, S. L. Salazar, Z. Rao, M. Arici and W. Wei, *Sol. Energy Mater. Sol. Cells*, 2021, **219**, 110792.
72 A. Ayyaz, G. Murtaza, A. El-Rayyes, M. Hussain, A. K. Alqorashi, I. Kebaili, M. B. Shakir and Q. Mahmood, *J. Inorg. Organomet. Polym. Mater.*, 2024, **34**, 5113–5131.
73 M. A. Rehman, J. ur Rehman and M. B. Tahir, *J. Phys. Chem. Solids*, 2023, **181**, 111443.
74 R. W. Birkmire and B. E. McCandless, *Curr. Opin. Solid State Mater. Sci.*, 2010, **14**, 139–142.
75 J. Tauc and A. Menth, *J. Non. Cryst. Solids*, 1972, **8**, 569–585.
76 P. Makuła, W. Pacia and M. Macyk, *J. Phys. Chem. Lett.*, 2018, **9**, 6814–6817.
77 Y. Li, M. Cui, H. Yan, Y. Yu, M. Li, X. Li, L. Chu, B. Jiang and M. Qin, *Materials*, 2018, **11**, 1809.
78 J. F. Nye, *Physical Properties of Crystals: Their Representation by Tensors and Matrices*, Oxford university press, 1985.
79 W. Voigt, *Lehrbuch der Kristallphysik (Textbook of crystal physics)*. BG Teubner, Leipzig und Berlin, 1928.
80 A. Reuss and Z. Angew, *Math. Mech*, 1929, **9**, 49–58.
81 R. Hill, *Proc. Phys. Soc. Sect. A*, 1952, **65**, 349.
82 S. F. Pugh, *London, Edinburgh Dublin Phil. Mag. J. Sci.*, 1954, **45**, 823–843.
83 M. N. Tripathi, A. Saha and S. Singh, *Mater. Res. Express*, 2019, **6**, 115517.
84 D. J. Lipomi and Z. Bao, *Energy Environ. Sci.*, 2011, **4**, 3314–3328.
85 G. N. Greaves, A. L. Greer, R. S. Lakes and T. Rouxel, *Nat. Mater.*, 2011, **10**, 823–837.
86 M. E. Eberhart and T. E. Jones, *Phys. Rev. B*, 2012, **86**, 134106.
87 C. M. Zener and S. Siegel, *J. Phys. Chem.*, 1949, **53**, 1468.
88 R. Gaillac, P. Pullumbi and F. X. Coudert, *J. Phys. Condens. Matter*, 2016, **28**, 275201.
89 R. Musembi and M. Mbilo, *AIP Adv.*, 2023, **13**, 115218.
90 O. L. Anderson, *J. Phys. Chem. Solids*, 1963, **24**, 909–917.
91 M. Maoz, Z. Abbas, B. Shah and V. Lughi, *Sustainability*, 2025, **17**, 1820.
92 M. E. Fine, L. D. Brown and H. L. Marcus, *Scr. Metall.*, 1984, **18**, 951–956.
93 Q. Q. Liang, D. Y. Hu, T. Y. Tang, H. X. Gao, S. Q. Wu, L. Li and Y. L. Tang, *J. Mater. Res. Technol.*, 2023, **22**, 3245–3254.
94 D. H. Ren and X. L. Cheng, *Chinese Phys. B*, 2012, **21**, 127103.